Ion Cyclotron Resonance Heating of H-modes in the JET Mark I Divertor Configuration

C Gormezano, V P Bhatnagar, M Bures, G Cottrell,
L-G Eriksson, B Fechner, L Horton, P Lamalle, J Jacquinot,
M J Mantsinen G Matthews, E Righi, F G Rimini, M Simon,
A C C Sips, D F H Start, K D Zastrow.

JET Joint Undertaking, Abingdon, Oxfordshire, OX14 3EA, UK.

1. INTRODUCTION

High power fast waves are routinely used in Tokamaks either in the Ion Cyclotron Resonance Heating (ICRH) regime or, by adjusting the frequency to avoid this powerful resonance, in the electron damping regime (Landau and Transient Time magnetic pumping). ICRH is a well established method for plasma heating in a variety of plasma conditions. These include high performance plasmas such as H-modes in JET[1] and ASDEX [2], high β_p VH modes in JET [3] and shear reversal configurations produced by pellet enhanced H-modes in JET [4] The data base on fast wave electron and ion current drive has expanded rapidly during the last five years. Electron current drive by a combination of transit time magnetic pumping and electron Landau damping is now a proven method [5,6,7,8] for driving current in the plasma centre (DIII-D, Tore Supra, TFTR) while minority ion current drive has been successfully employed on JET to change the current density gradient at the q=1 surface and control the sawtooth period [9]. These heating and current drive experiments have formed the basis to support ICRH as one of the main candidate methods for additional heating on ITER. In addition, when RF waves are damped on minority species, or on majority species at harmonics of the ion cyclotron frequency, a large population of well confined fast ions whose energy can extend up to a few MeV, can be created. They constitute the closest way to simulate the behaviour of alpha particles in reactor type devices. This paper presents ICRH physics aspects mostly related to this simulation.

Recently, JET has been modified to accommodate a new divertor, the Mark I, which is the first in a series of divertors being tested for ITER. This is the first stage of a programme of divertor optimisation coupled with studies of high performance plasmas in ITER-like geometry. A new set of antennas, the A2 antennas, have been designed to match the new magnetic configuration [10]. After installation of the Mark I divertor, the behaviour of plasmas in H-mode was found to be somewhat different to that of previous campaigns in JET. In particular, high additional heating power produces plasmas with ELM relaxations of large amplitude, unless specific configurations are used with high flux expansion on the divertor tiles, high triangularity and high shear at the edge [11]. Despite specific coupling problems related to ELMs, up to 16.5MW of ICRH power has been launched into a diverted plasma. With combined additional ICRF + NBI heating power, a maximum of 32MW, including 15MW of ICRH power, was injected in a high density radiative divertor plasma [12].

The purpose of this paper is to present the new features which have been observed in H-modes with ICRH in the Mark I divertor configuration on JET. The paper is arranged as follows. In section two we give a brief description of the JET A2 antennas and summarise their operating characteristics. Section 3 presents the H-mode plasma parameters achieved with ICRH only in high flux expansion 3MA and 5MA discharges, with 16.5MW of ICRH in

1

2.5MA "gas box" divertor [13] simulation experiments and with 32MW of combined ICRH (15MW) and NBI (17MW) in high density radiative divertor discharges. The plasma rotation induced by ICRH and rapid spin-up of the plasma at the H-mode transition are discussed in section 4. The results of H-mode threshold measurements are compared with those achieved with NBI in section 5. Third harmonic heating of deuterium plasmas has produced the maximum neutron yield ($\sim 10^{16}$/s) with ICRH and these results provide a strong test of ICRH modelling in terms of both the damping and the fast ion tail production. The results are described and compared with PION code simulations in section 6. On-axis ICRH in hot ion H-modes created by NBI increased the global thermal energy confinement by up to 30% and increased the rate of rise of the neutron production. Detailed results of these experiments and their interpretation are presented in section 7. Record electron temperatures of up to 15keV have been achieved both with combined heating in hot ion H-modes and with ICRF only in high flux expansion 3MA H-modes. These data and the results of transport analysis studies are discussed in section 8.

2. THE A2 ANTENNAS

A new set of "A2" antennas were installed in JET in 1993 to match the new plasma configuration as shown in Fig.1. These antennas are arranged in four arrays each having four current straps at nearly constant pitch. Each strap is fed by an independent power source. A chosen spectrum can be launched by appropriate phasing of the power sources. Each array, has a slotted central septum and an open beryllium screen. A module shown installed in the torus can be seen in Fig.2. The side walls of the antennas are also slotted in order to optimise phased operation of the array. Poloidal limiters with a large poloidal span are located on each side of a module. With such a 4-strap antenna arrangement, the excited $k_{//}$ spectrum is much narrower than the one achieved with the previous 2-strap A1 antennas [14] and a large variety of wave spectra can be excited as shown in Fig.3.
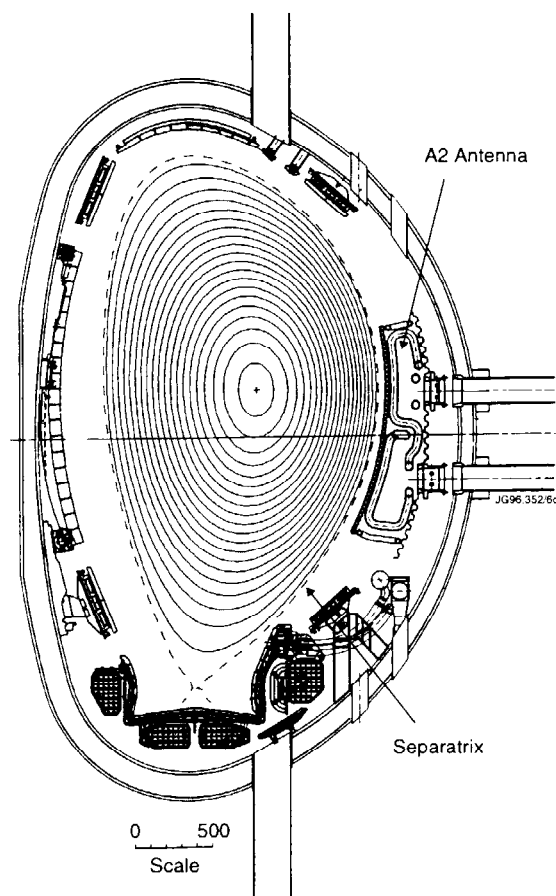

Fig.1: Cross section of the JET tokamak showing the geometrical relationship of the A2 antennas to a typical divertor plasma.
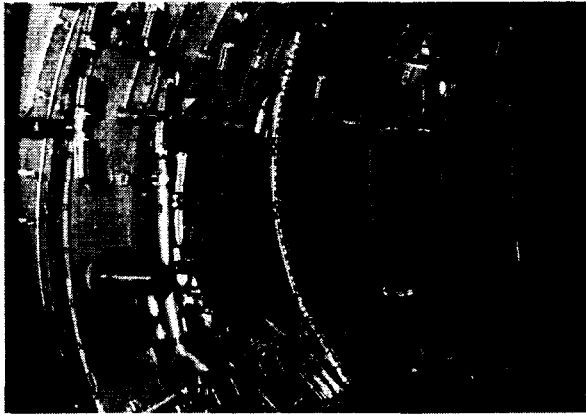
Fig.2: View of a single 4-strap A2 antenna module inside the JET vacuum vessel. Note the angled screen bars which align closely with the magnetic field lines.
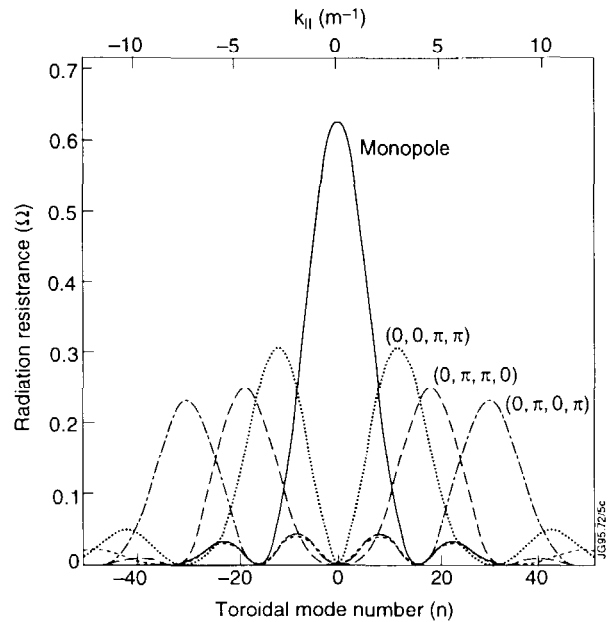
Fig.3: Parallel wavevector spectra of waves launched by the A2 antenna for various phasing of the current straps.

The early operation of the A2 antennas has been described previously [12]. Extensive coupling studies, as well as scattering matrix measurements, have been carried out for frequencies ranging from 32MHz to 56MHz, and have shown that the coupling resistance of the inner strap was significantly lower than for the outer straps for frequencies below 50MHz. This imbalance was caused by a mismatched crossover link which connects the inner strap to the main transmission line. The effect of the coupling asymmetry on the power coupled to the plasma was minimised by operating with equal voltages (up to 30kV) on the antenna straps and by using high frequencies (typically 52MHz) which gave the least imbalance. Since the 1995 campaign extra capacitance has been added to the crossover link to bring its characteristic impedance as close as possible to that of the main transmission line.

The data base generated by the coupling studies revealed an interesting feature in the dependence of the loading resistance, R_c, on the distance between the plasma separatrix and the poloidal limiter at different poloidal locations. Values of R_c plotted against this distance as measured at the midplane showed the usual decrease in coupling with distance as shown in fig.4. The behaviour of R_c versus the distance between the plasma and the limiter can be well reproduced with a predictive coupling code [15] using reasonable assumptions for the edge plasma density. Such a good agreement is only observed at f = 52MHz where the coupling resistances of the 4 straps are about equal. At other frequencies, similar agreement is only found for the outer straps. However, as shown in Fig.5, where R_c is plotted against the distance between the separatrix and the bottom of the poloidal limiter (for a narrow range of midplane separations) there is an increase in R_c with increasing distance. This effect was caused by the
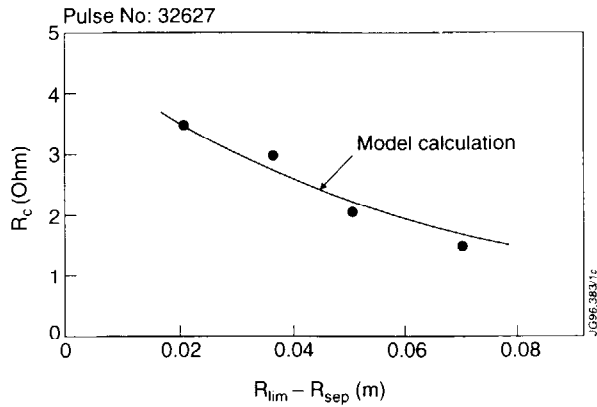
3

Fig.4: ICRF coupling resistance versus separation between seperatrix and limiter compared with model calculations in which the density at the separatrix was taken to be $10^{19}m^{-3}$ and the density decay length in the scrape-off layer was 1cm.
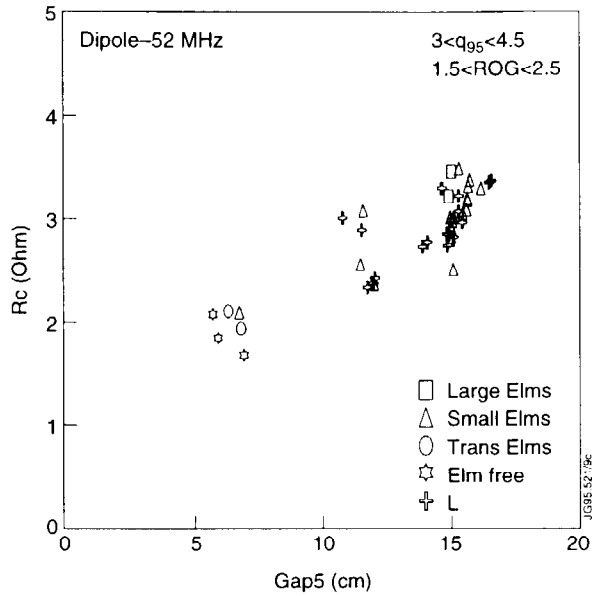

Fig.5: Increase in the coupling resistance as the gap between the lowest section of the limiter and the last closed flux surface is increased.

difference between the curvature of the last closed flux surface and the curvature in the bottom part of the poloidal limiters and can be understood in terms of field line connection length. For a fixed midplane separation, a large gap at the bottom of the poloidal limiter is created when the separatrix is more curved than the antenna screen. In this case field lines which pass close to the screen continue, unobstructed by any material surface, around the machine until they strike the divertor plates. The distance from screen to divertor along the field line, the "connection length" is typically 12m. In discharges with less curvature, the field lines passing close to the screen at the midplane can intersect the lowest section of the limiter giving a reduced connection length (~2m) with a correspondingly lower density at the screen and reduced coupling to the plasma. The lower part of poloidal limiters has been modified to eliminate this effect for the 1996 campaign.

The ICRH control system trips the generators if the reflected power to the tetrode output amplifier exceeds 4% of the forward power. Sudden changes in coupling such as those produced by ELMs can induce these trips. An example is shown in fig.6. The coupling resistance prior to the ELM is 1.5Ω and rises to 6.5Ω in 0.3 msec when a large
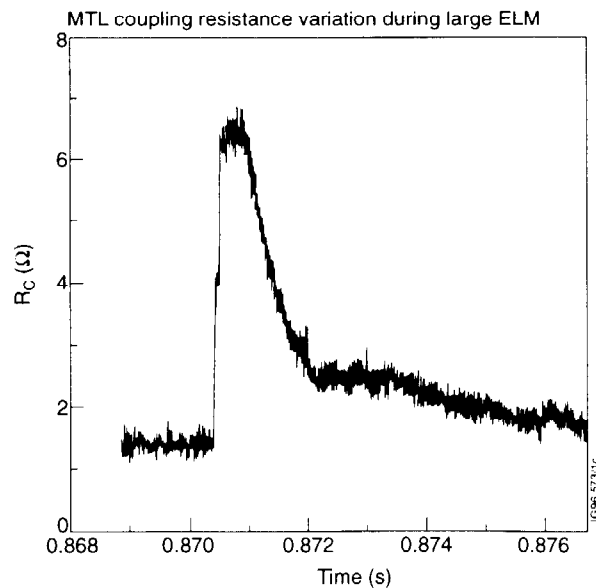

Fig.6: Variation in ICRH coupling resistance during a large ELM.

ELM occurs. The coupling subsequently decreases on a timescale of about 1 msec. The control system has been upgraded to re-apply the power after the ELM so that the power shut-down time is minimised (~4ms). The system was successfully tested only during the very last phase of the 1995 operations. However, as the ELM frequency increases beyond 20Hz the coupled power is reduced significantly. To overcome this problem a new wide band matching system is being developed at JET in which prematching elements and small (1%) but fast frequency changes are used to maintain a good match during the ELM.

3. HIGH PERFORMANCE PLASMAS

The magnetic configurations which have produced the best plasma performance measured in terms of high neutron yield, long ELM-free period and high central temperatures, are those with high triangularity and large flux expansion in the divertor chamber. An example is shown in Fig.7 where a central electron temperature of 14.5keV was achieved in an RF-only H-mode. The plasma current for this discharge was 3MA and the toroidal field was 3.2T. The ICRF frequency was 52MHz which produced hydrogen minority heating with the resonance located about 0.1m on the high field side of the magnetic axis. The initial RF power level of 10MW combined with 1.8MW of

Fig.7: An ICRF produced H-mode in which the central electron temperature reaches 14.5keV.

diagnostic neutral beams, produced the H-mode. In this configuration R_c is rather low and the antennas were operated at 30kV maximum voltage to deliver this power level. The ensuing ELMs subsequently tripped some of the generators. The RF power was stepped down to 7MW at t = 15s, the density decreased from 3.5 x 10^{19} m^{-3} to 2.5 x 10^{19}m^{-3} and the ELM activity almost disappeared. The central electron and ion temperature reached 14.5keV and 6keV, respectively. The corresponding $T_e(r)$ profiles from the ECE and LIDAR Thompson scattering diagnostics are shown in Fig.8. Note that neither diagnostic measures at the exact plasma centre; the horizontal line of sight of the LIDAR system is about 0.3m below the magnetic axis whereas the ECE measures 0.1m above the plasma centre.

An example of an RF H-mode in a 5MA discharge is shown in Fig.9. The RF power level was 8.5MW at its maximum which produced a plasma stored energy of over 7MJ. The electron temperature reached 8.5keV at a plasma density of 4 x 10^{19}m^{-3}. Note that the first large
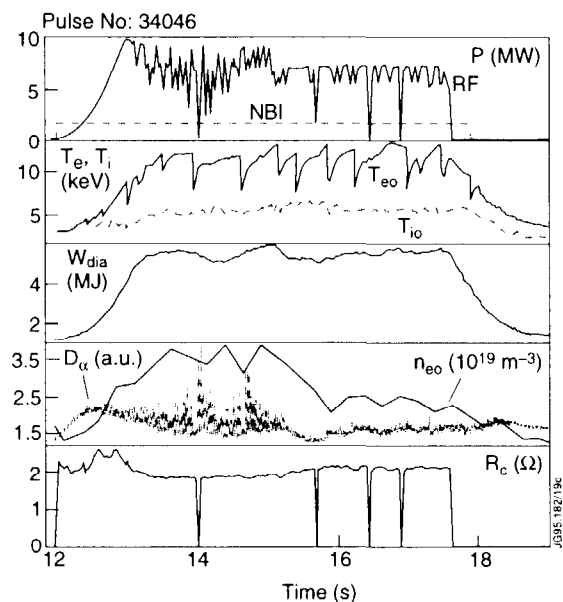
5

ELM occurs more than an energy confinement time after the transition to the H-mode, a situation which is typical of RF H-modes. The confinement enhancement factor with respect to ITER-89P scaling reaches a value of 1.8.
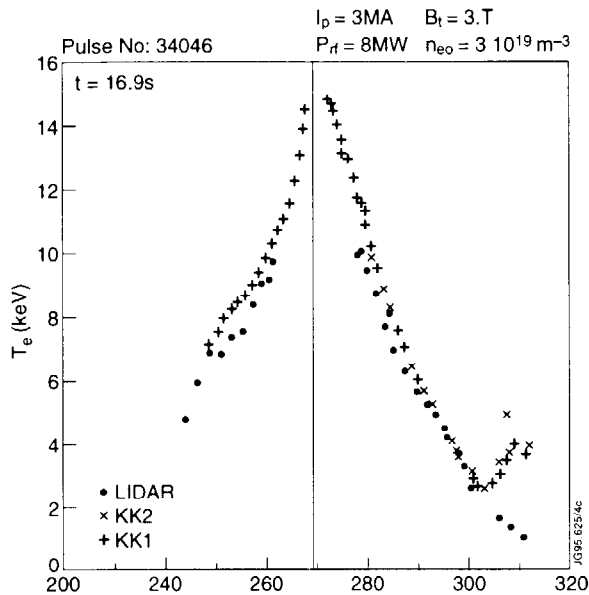

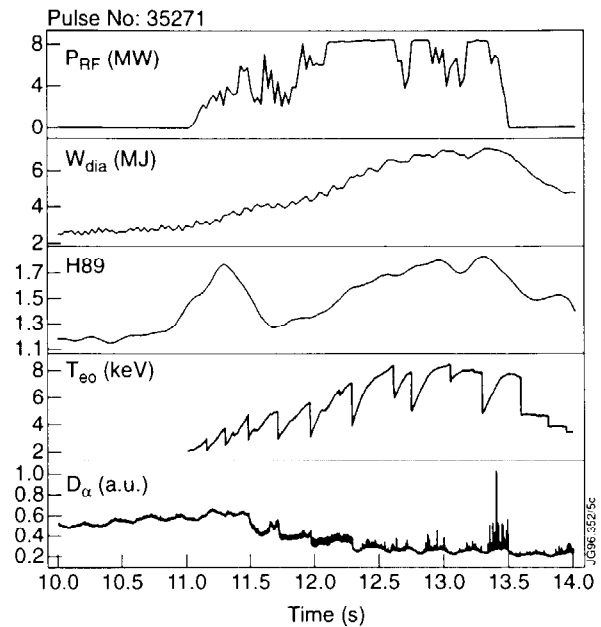Fig.8: Electron temperature profiles given by ECE and LIDAR diagnostics for pulse 34046.

Fig.9: An example of an ICRF generated H-mode in a 5MA divertor plasma with a stored energy of 7.5MJ for an RF input power of 8MW.

The maximum ICRF power achieved so far with the A2 antennas was 16.5MW and was coupled with $0\pi\pi0$ phasing to a 2.5MA high X-point divertor plasma configuration which is compatible with a gas box type of divertor. The evolution of parameters is shown in Fig.10. The initial power level of 10MW establishes the H-mode with an enhancement factor of 2. A monster sawtooth is created at t = 14s and lasts for 2.5s as the power is ramped up to 16.5MW. The central electron temperature remains steady at 7keV as the density increases from 3 x 10^{19}m^{-3} to 5 x 10^{19}m^{-3}. In this case also, significant ELMs only appear 1.5s after the L-H transition. The oscillations in the D_α signal are due to sweeping of magnetic field lines across the divertor plates.
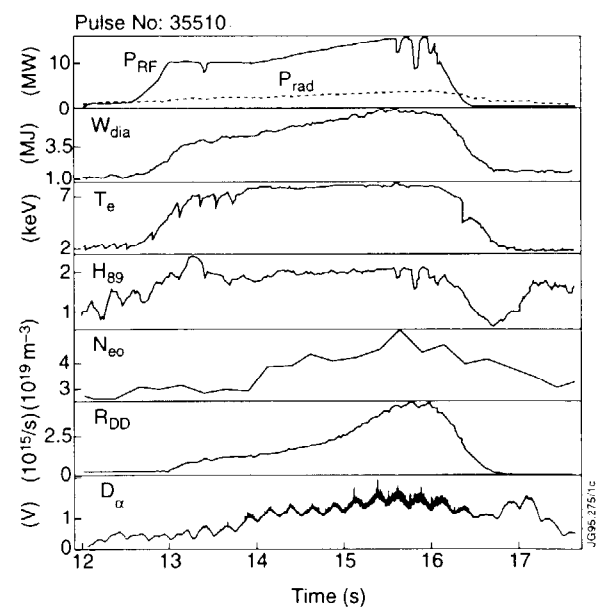

Fig.10: An H-mode produced by 16.5MW of ICRH in a 2.5MA "gas box" type divertor plasma with a central density of 5 x 10^{19}m^{-3}. The H-factor over L-mode is 2.0.

6

Strongly radiating divertor plasmas provide a good target for ICRH since the ELMs are "grassy" and the average coupling resistance is slightly higher at around 3Ω for $0\pi\pi 0$ phasing. A combined power of 15MW of H-minority ICRF and 17MW of D^0 NBI was injected into such a plasma with I_p = 2.5MA, and B_T = 3.4T as shown in Fig.11. The RF frequency was 51.3MHz to give central heating. The neutral beams were injected prior to the RF in order to establish an H-mode with "grassy" ELMs. The density was increased to 6.4 x $10^{19}m^{-3}$ as the RF power was ramped up and nitrogen was injected to produce impurity seeding such that 60% of the input power was radiated in the divertor region. At maximum power, the stored energy reached 7MJ corresponding to peak electron and ion temperatures of 8.5keV and 5keV, respectively.
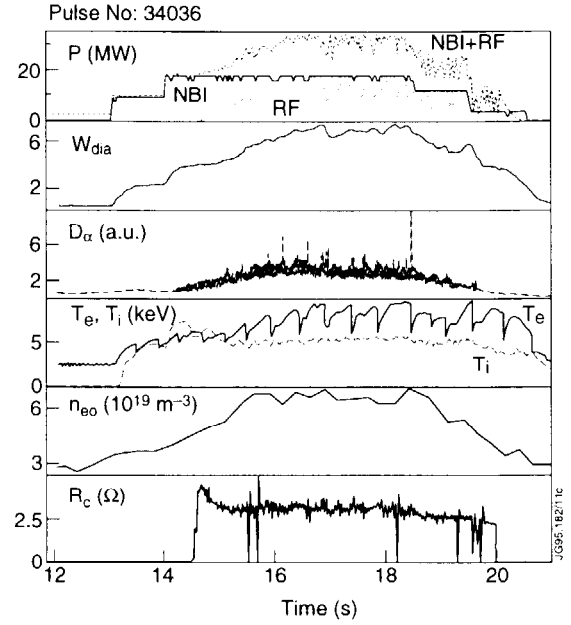

Pulse No: 34036

Fig.11: Combined ICRF and NBI heating in a high density 2.5MA, 3.4T radiative divertor discharge. The total power is 32MW of which 60% is radiated in the divertor region.

At $t = 16s$ the density reaches 6.5 x $10^{19}m^{-3}$ and the beam heating profile becomes almost flat (Fig.12), according to PENCIL code calculations [16] due to lack of penetration. In contrast, the ICRF power deposition profile is predicted to be highly peaked on axis by the BRAYCO [17] ray tracing code as shown in Fig.13 since the fast wave has good accessibility at high density. Theoretically, strong centrally localised heating should produce both enhanced central energy density and increased global confinement since the majority of the power is placed in a region of minimum thermal conductivity. The observed improvement in τ_E is revealed in the time development of the normalised confinement time or H-factor, which allows deposition effects to be separated from changes brought about by changes in power, plasma parameters and geometry. The H-factor based on ITERH93-P scaling of the thermal energy content is defined by:

$$H93 = \tau_E/\tau_{93}$$

where

$$\tau_{93} = 0.035 \, I_p^{1.08} \, n^{0.17} \, B_t^{0.32} Q_L^{-0.67} R^{1.79} \varepsilon^{-0.11} \kappa^{0.66} M^{0.4}.$$ (1)
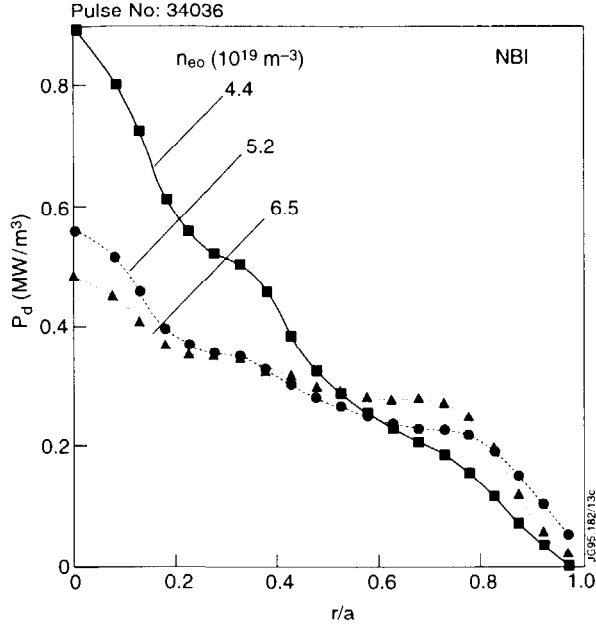
7

Fig.12: Neutral beam power deposition profiles for various densities during the radiative divertor pulse, shown in fig.10.
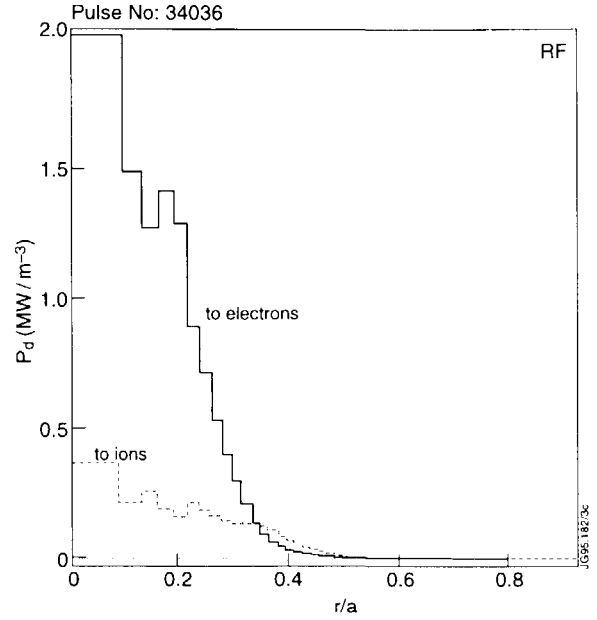
Fig.13: ICRF power deposition profile for pulse 34046 calculated using the ray tracing code BRAYCO. The RF scheme used minority hydrogen heating at the fundamental resonance which gave predominantly electron heating by collisional transfer.

In equation (1), I_p(MA) is the plasma current, $n(10^{19}m^{-3})$ is the density, B_t(T) is the toroidal field, Q_L(MW) is the loss power, R(m) is the major radius, ϵ is the inverse aspect ratio, κ is the elongation and M is the atomic number of the plasma ions. The evolution of H93 for discharge 34036 is shown in Fig.14. During the first stage of the beam heating the H-factor is 0.42 and the plasma is in L-mode. The H-mode is triggered by the second step in beam power, as shown by the behaviour of the ELMs in Fig.11, and the H-factor increases to 0.49 at t = 15s. By this time the density has risen to 6 x $10^{19}m^{-3}$ and the beam heating profile has broadened (Fig.12). As the ICRF power is ramped up, the H-factor further increases to a value H93 = 0.57. Thus the ICRF central power deposition produces a 16% increase in normalised global energy confinement.

This result is compared with theoretical expectations using a heat transport simulation of discharge 34036. The power scaling of τ_{93} is commonly assumed to be due to a temperature dependence of the thermal conductivity χ. The particular case of $\tau_{93} \propto Q_L^{-0.67}$ implies the relation $\chi \propto T^2$. To take this dependence into account, we have solved the heat diffusion equation

$$-\frac{1}{r}\frac{\partial}{\partial r}(n\chi\frac{\partial T}{\partial r}) + P_d(r) = 0 \qquad (2)$$

8

in a iterative way. Initially the $\chi(r)$ profile was chosen to reproduce the observed average temperature $T = (T_e + T_i)/2$ for the NBI only phase at 15s, for a density of 6 x 10^{19}m^{-3}. This χ profile was then used to determine an initial temperature profile for the ICRF + NBI case using the heating profiles shown in Fig.12 and Fig.13. The conductivity was then renormalised at each radius according to $\chi \propto T^2$ and the diffusion equation solved again. This procedure was repeated until the temperature profile converged, typically after 3 iterations. The results are shown in Fig.15.
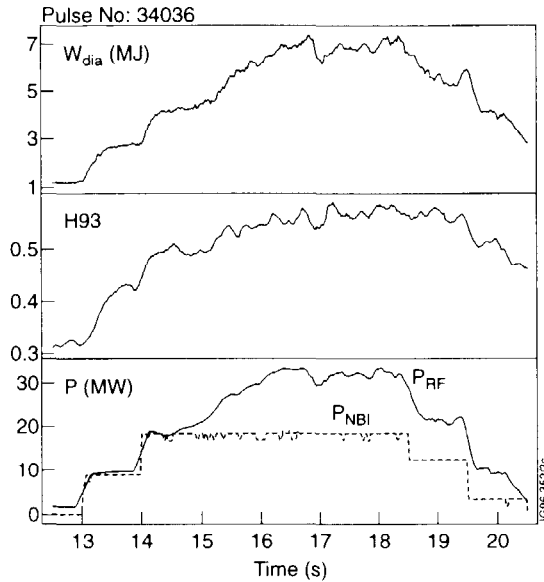

Fig.14: Evolution of the ITER-H93P enhancement factor showing about a 16% increase at t = 15.2s due to the central power deposition of the ICRH.

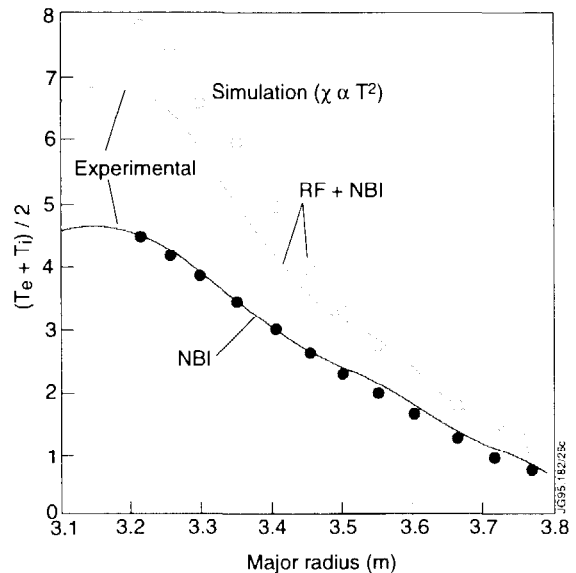Fig.15: Simulated temperature profiles for pulse 34046 using a transport code and a scaling of $\chi\alpha T^2$ which is compatible with ITER-H93P power scaling.

The initial χ profile was obtained from the fit to the T(r) profile with NBI (solid points). The calculation for the combined heating phase agrees well with the measured temperature profile with a slight overestimate in the centre. This profile was used to calculate the thermal energy content and the H-factor. Compared with the beam heating phase at $n_e = 6$ x 10^{19}m^{-3}, the H-factor with combined heating is predicted to increase by 18% which is in excellent agreement with the measured increase of 16%. It should be noted that $\chi \propto T^2$ is a particularly deleterious scaling, a fact reflected by the poor H-factors achieved by radiative divertor plasmas; $H_{93} \sim 1$ represents an ELM-free H-mode.

4. TOROIDAL PLASMA ROTATION

Measurements of toroidal rotation near the plasma centre (r/a $\equiv$ 0.3) have been obtained during RF-only L and H-modes using a high resolution X-ray crystal spectrometer [18,19]. Such measurements are particularly interesting since they have revealed changes in angular frequency ω and momentum density l to be clearly correlated with plasma phenomena like the transition to

9

H-mode and giant ELMs. Such effects are usually more difficult to detect with NBI based charge-exchange diagnostics due to the fact that the neutral beams transfer substantial torque to the plasma. Theoretical interpretation of such measurements is still in progress but already from the existing observations it is possible to speculate about the possible mechanism at work during RF-only H-modes. This is particularly important in view of the possible implications on confinement during H-modes in ITER.

A typical example of a rotating RF H-mode is given in Fig.16 which shows the behaviour of the rotation measured at r/a = 0.3 during RF heating. Concomitant with the transition into a practically ELM-free H-mode is a sudden increase in the rate of rise of angular frequency, ω. This increase is closely associated with the L-H transition itself and not with any change in the RF power. According to the neo-classical expression for the rotation velocity [20], an ion pressure gradient gives a contribution in the direction of the plasma current, i.e. consistent with the experimental observation. The contribution is of the order $v_{\phi nc} \sim \dfrac{qv_i^2}{a\varepsilon\omega_{ci}}$. where v_i is the ion

Fig.16: Increase in the plasma rotation at r/a - 0.3 as an RF-only H-mode is formed in a 3MA, 2.8T discharge.

thermal velocity, a is the mnior radius, ε is the inverse aspect ratio and ω_{ci} is the cyclotron frequency of the bulk ions. However, there is also a contribution from the radial electric field. Since the radial electric field is not measured, it is difficult to assess its influence. Furthermore, owing to the damping by neutral impurities in the plasma (and possibly other anomalous effects) the measured rotation speed is expected to be lower than predicted by neo-classical theory, which is also consistent with observations $v_{\phi exp}/v_{inc} \sim 0.5$. For a plasma heated by ICRF the situation is even more complicated since the ICRF wave can transfer momentum to the plasma. The background plasma absorbs this momentum via collisions with the resonating ions and through a $\overline{J}_r x \overline{B}_p$ torque, where $\overline{J}_r$ is a radial background plasma current and $\overline{B}_p$ is the poloidal magnetic field. The radial background plasma current arises because of the ICRF induced radial diffusion of resonating ions [21, 22], it simply ensures that quasi neutrality is maintained. A more detailed discussion of the RF induced rotation is given in ref.19 The wave induced torque is in the direction counter to the current. Consequently, the wave induced torque should damp the rotation produced by the ion pressure gradient. To make a realistic estimate of this counter torque is very difficult, it would require detailed calculations of the distribution function of the resonating ions with at least a 3D
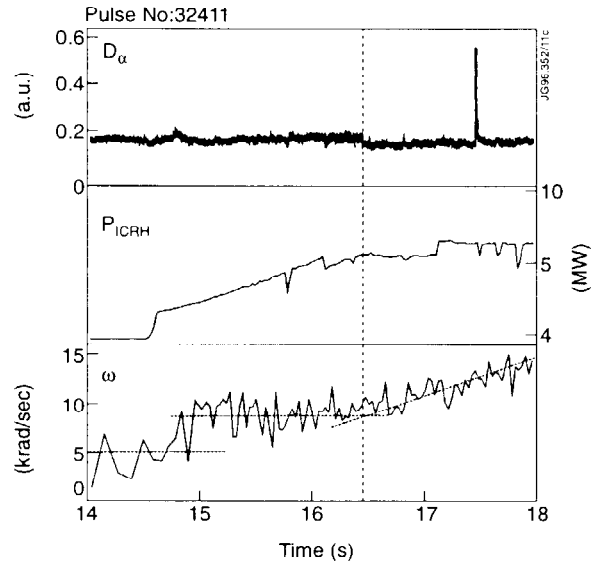
Fokker-Planck code. This is outside the scope of the present paper. The experimental results indicate that the ion pressure gradient mechanism is the dominant effect. In this case the angular momentum should correlate well with ∇P, which is closely related to the central ion pressure. Figure 17 shows the good correlation between l and $n_i T_i$ before and after the L-H transition.

The influence of ELMs on rotation is shown in Fig.18. As the RF power is applied, the plasma begins to accelerate until the speed has increased by ~4 krads/s and a steady state is attained just before the L-H transition. After this transition a further acceleration occurs until the first large ELM at t = 20s. At this point the acceleration stops briefly. After
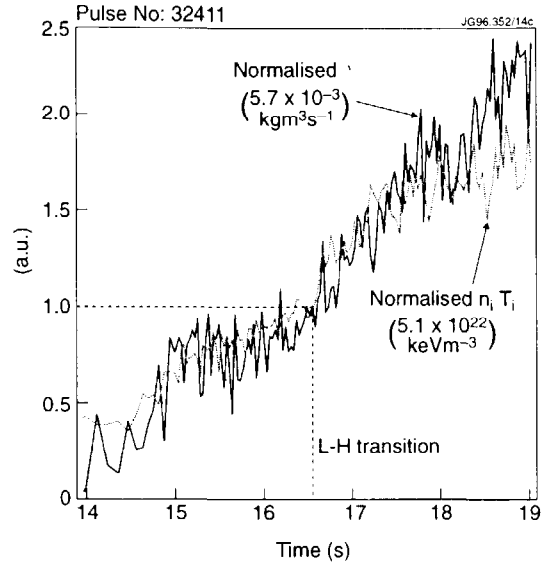

Fig.17: Angular momentum increase in pulse 35271 which follows the increase in ion pressure in agreement with the prediction of neo-classical theory.
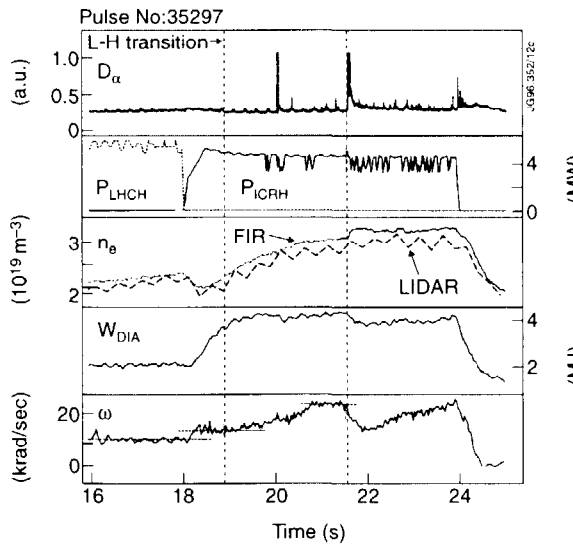

Fig.18: The effect of a large ELM in reducing the angular velocity at 21.6s during pulse 35297 whichis a 3MA, 2.8T discharge with the ICRH resonance approximately 0.2m on the high field side of the magnetic axis.
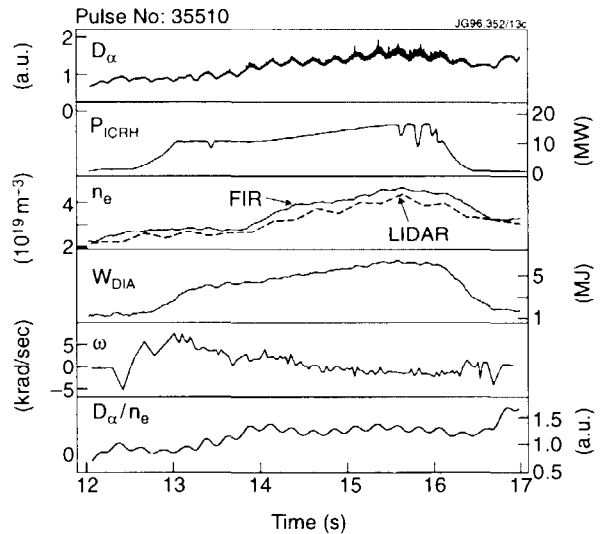

Fig.19: Reduction in rotation produced by strong gas injection in a "gas box" type discharge.

the ELM, the rotation increases again until a steady state is reached at 21s with $\omega \sim$ 22krad/s. A giant ELM occurs at 21.5s and the plasma rotation slows rapidly while the ELM is present. When the perturbation is dispersed, the plasma accelerates again until the end of the RF pulse.

11

Clearly a giant ELM can produce a substantial perturbation as far into the plasma as r/a = 0.3 confirming other measurements [23]. The rotation can also be reduced if strong gas puffing is used as shown in Fig.19. Discharge 35510 has a large gas input applied from t = 13s until t = 17s. During this time the rotation speed steadily decreases apart from a small recovery at t = 13.7s when the H-mode is formed.

5. H-MODE THRESHOLD WITH ICRH ONLY

The ICRF H-modes form an important part of the 1995 JET contribution to the ITER threshold database [24]. In addition they provide a means of investigating H-modes produced and heated by high energy fast ions, thereby simulating H-modes in a reactor sustained by α-particles. H-modes in JET have been obtained for a large variety of plasma shapes for a range of currents from I_p = 1MA to I_p = 5MA, for toroidal field values from B_T = 1.6T to B_T =3.5T and with either $0\pi0\pi$ (dipole) or $0\pi\pi0$ phasing of the ICRF antenna. The data presented in this section have been obtained following the selection criteria of the ITER threshold database. Thus L-H transitions are represented by data-points taken ~30 msec before the actual H-mode transition, and averaged over a ±25 msec interval.

A subset of the ICRF data is shown in Fig. 20 for values of the magnetic field B_T varying from 2.8T to 3.45T. This subset can be compared directly with results of threshold investigations with NBI only which were dedicated to determining the density scaling of the threshold power. For the ICRF data the scaling of P_{TH}, expressed as total (auxiliary plus ohmic) coupled power, is roughly linear with the central line-averaged density n_e, although the B_T variation introduces scatter in the data. Analysis of the 3MA/3T NBI group of data (at constant B_T) shows, however, that the n_e dependence might not be so simple. The high density plasmas appear to have an abnormally high threshold. Degradation of the power threshold due to substantial cooling of the plasma edge caused by strong fuelling with neutrals, necessary in order to raise sufficiently the target density, could be one possible cause.
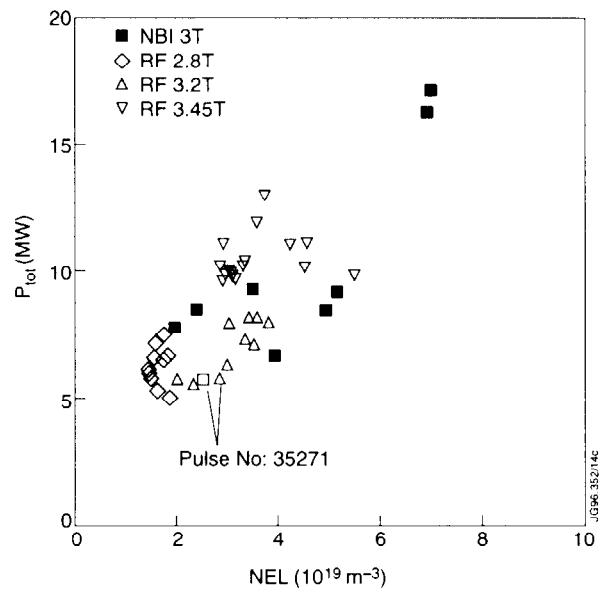

Fig.20: Power required to form H-modes versus electron density for both RF and NBI heating in discharge with similar values of toroidal field.

As far as the dependence of P_{TH} on the heating system is concerned, Fig.20 also shows that NBI and ICRF are roughly equivalent. This is particularly evident from the example of

12

discharge 35271 (3.2T/5MA), where two consecutive H-modes are formed, the first with ICRF heating only, and the second with NBI heating only (Fig.21). During the RF phase the D_α signal decreases in steps and does not provide an unambiguous signature of the L-H transition. However the increase in the rotation does show clearly that the transition occurs at t = 11.6s. The NBI H-mode is formed during the low power phase of the heating and occurs at the same power level as the RF H-mode, but at a lower density; $n_e = 3 \times 10^{19} m^{-3}$ compared with $3.5 \times 10^{19} m^{-3}$ for the RF case. It is also to be noted that the ELM activity is generally lower for ICRH only H-modes than for NBI only H-modes as shown in Fig.21: the amplitude and frequency are lower. This can be explained by the absence of fuelling at the edge with ICRH. The pressure at the edge, which is thought to be triggering the ELMs, is less likely to increase in this situation.

A linear dependence of P_{TH} on B_T, n_e and possibly a stronger variation with major radius R is believed to be valid [24]. The power threshold, expressed as $P_{LOSS} = P_{TOT} - dW_{DIA}/dt$, is plotted in Fig.22 against the product $n_e B_T R^{2.5}$. It is evident that the measured threshold is approximately represented by the scaling law $P_{TH} = 0.3\ n_e B_T\ R^{2.5}$ which also well represents the combined JET-DIII-D data [24].
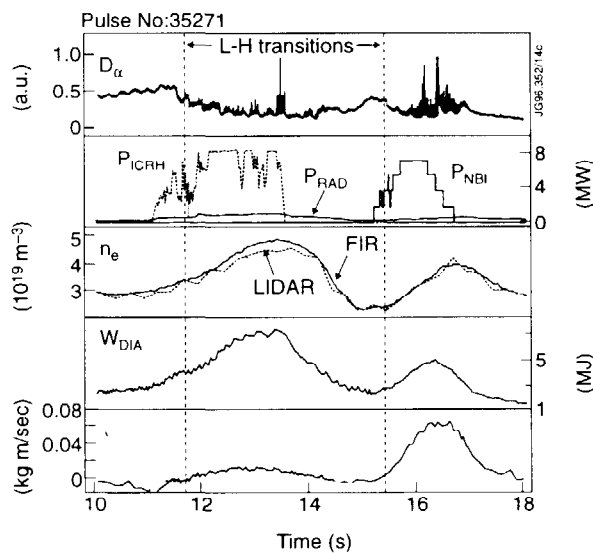

Fig. 21: Direct comparison between RF and NBI in the same discharge showing that similar power levels are required to access the H-mode.
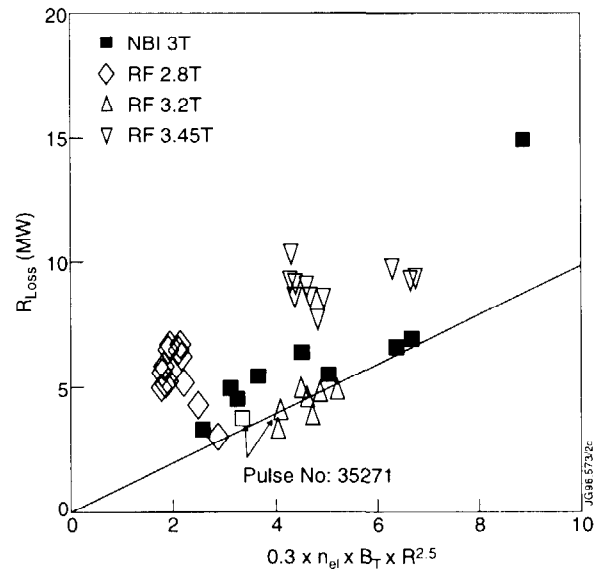
Fig.22: Power through the seperatrix versus $0.025 n_e B_T S$. Note the deviation from this scaling at high density (and high gas influx).

6. THIRD HARMONIC ICRF HEATING

Studies have been carried out of central ICRF heating at the third harmonic deuterium resonance with deuterium as the main plasma species. In typical JET plasmas the initial damping on the thermal ions is considerably weaker than direct electron damping. However, a high energy tail soon develops and the ion damping becomes the predominant absorption mechanism. The time

13

behaviour of the neutron yield from non-thermal D-D reactions provides a stringent test of any simulation. In particular the fraction of power absorbed by the ions and the development of the high energy tail must be calculated self-consistently, and finite orbit sizes have to be taken into account.

The absorption mechanism for heating with $\omega = n\omega_{ci}$, $n \geq 2$, is a finite Larmour radius effect. An ion passing through a cyclotron resonance receives a change in its perpendicular velocity, $v_\perp$, according to

$$\Delta v_\perp \sim v_\perp \left[E_+ J_{n-1}\left(\frac{k_\perp v_\perp}{\omega_{ci}} \right) + E_- J_{n+1}\left(\frac{k_\perp v_\perp}{\omega_{ci}} \right) \right],$$

where E_+ and E_- are the left-hand and right-hand polarised components of the wave electric field, respectively, and $k_\perp$ is the perpendicular wave number. From this expression one can see that for $n \geq 2$ the wave particle interaction is weak at low perpendicular velocities and increases with $k_\perp v_\perp/\omega_{ci}$ until a maximum is reached, which for typical JET parameters occurs in the MeV range. As a result, the damping for thermal plasmas is normally weak. Furthermore, the distribution function of the resonating ions is only weakly affected in the low energy range but tends to have a non-Maxwellian tail with a relatively small number of very energetic ions. The development of a tail plays a significant role for the absorption strength. Since the power per particle varies as $(k_\perp \rho_i)^4$ plus higher order terms (at least for $k_\perp \rho_i < 1$, where ρ_i is the ion Larmour radius. As the tail evolves, more ions interact strongly with the wave and the absorption strength is enhanced; this leads to a stronger tail and more absorption. It is therefore in principle possible to have significant damping with higher harmonic interaction even if the distribution function of the resonating ions initially is Maxwellian. However, the RF power must be high enough to create a substantial tail and the target plasma sufficiently hot so that the higher harmonic damping is not too weak initially. In addition, it is necessary to have a large enough machine which can confine the energetic ions giving rise to the enhanced absorption. These conditions are usually not fulfilled in smaller machines. Third harmonic heating has consequently almost only been observed in discharges where the waves interact with neutral beam injected ions [25, 26]. In JET, however, the above conditions can be met.

The experiments carried out on JET used deuterium plasmas with a magnetic field of 2.2T in the plasma centre and a plasma current of 2MA. ICRF power was applied with a frequency of 51MHz corresponding to a third harmonic deuterium resonance in the centre of the plasma. The time evolution of the major plasma parameters for discharge 35525 are shown in Fig. 23. The ion temperature remains fairly low (~2.5keV) when ICRF power is applied. The DD neutron rate, on the other hand, increases strongly during the ICRF heating phase, reaching the record neutron rate of $10^{16}s^{-1}$ for ICRF alone in JET. Because the ion temperature remained low, the strong increase in the DD neutron yield indicates that a tail of fast deuterium ions has
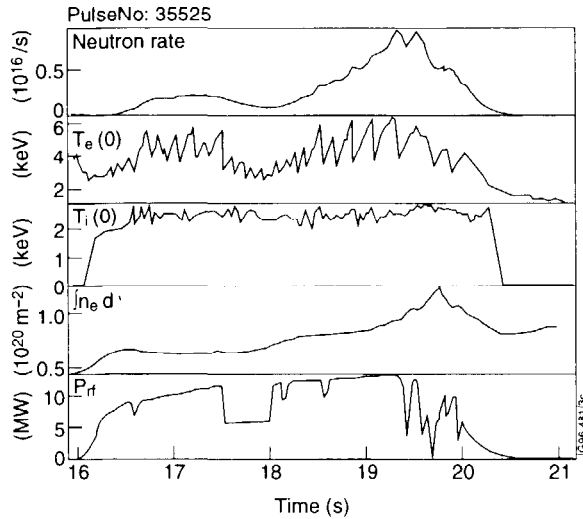
14

PulseNo: 35525

Fig.23: Evolution of plasma parameters during third harmonic cyclotron heating of deuterium.

been created. Further evidence for this interpretation is given in Fig.24, where the line-integrated deuterium distribution function, measured with a high energy neutral particle analyser [27], is shown for discharge 35525. To put the high neutron yield in perspective, we have compared the discharge with a neutral-beam-heated discharge having similar power level, plasma current and magnetic field. The result is shown in Fig.25. Both discharges produce about the same neutron rate, but in different ways. The DD fusion cross-section increases by almost an order of magnitude between the energy range where the beam ions are injected and its maximum at around 3MeV. Neutral beam heating gives rise to a high neutron rate because it creates a fairly high ion temperature and many ions at intermediate energies. Third harmonic heating, on the other hand, produces a tail of a few very energetic deuterium ions near the peak of the fusion cross-section.
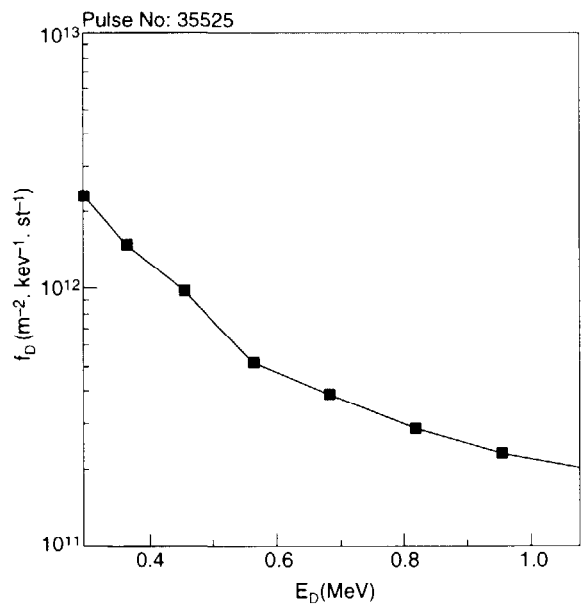

Fig.24: Measured deuterium tail distribution using the JET high energy neutral particle analyser during third harmonic heating.
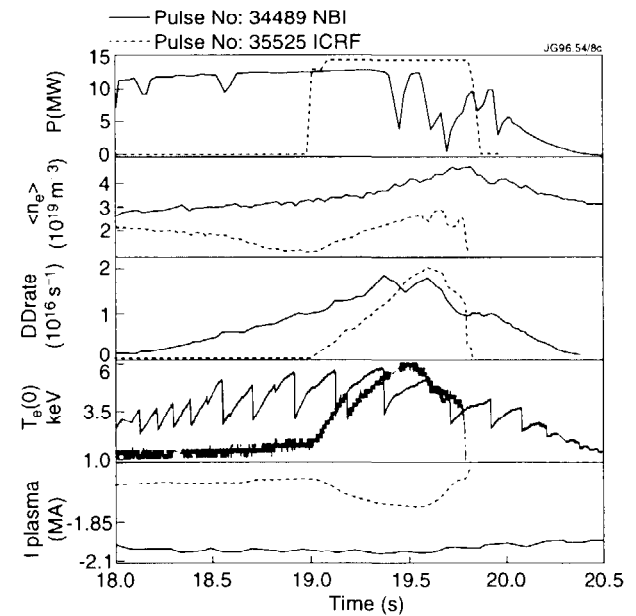

Fig.25: Comparison between the DD reaction rates produced by similar power levels of NBI and third harmonic ICRH.

In order to estimate the amount of power absorbed by third harmonic damping in discharge 35525, the discharge has been simulated with the PION code [28,29]. This code, which reads all its input date from the JET experimental data base, takes into account the

15

enhanced absorption due to tail formation and also includes effects due to finite orbit widths. The latter effects played an important role in discharge 35525 since the current was low and very energetic ions were created. It should be noted, however, that the PION code does not include all effects which are relevant for this discharge. In particular, RF-induced spatial diffusion and redistribution of fast ion during sawtooth crashes are not taken into account. Spatial diffusion is, however, of importance for the very energetic ions created during third harmonic heating, and the sawtooth-induced redistribution of fast ions is expected to affect the absorption strength at least transiently.

The comparison between the measured and calculated reaction rates is shown in Fig.26. The agreement is reasonably good. To achieve this agreement, two additions to the code have been made: a parasitic absorption of 4% per pass at the plasma edge, which only plays a role initially when the damping is very low, and a particle loss term, which removes particles above 4MeV, i.e. particles that were not confined in the plasma. As mentioned above, the strong increase in DD neutron rate during ICRH indicates that a tail of energetic deuterium has been created. According to the simulation, the rise in the neutron yield at the end of the RF phase is due to the increasing deuterium density. As a result of the increasing density the fast ions become less energetic, i.e. less orbit losses occur while the fraction of fast ions stays roughly constant. The DD fusion reactivity, which is dominated by reactions between fast and thermal ions, therefore increases with the bulk deuterium density. To maximise the DD fusion reactivity, the RF power and the deuterium density should be increased simultaneously. In Fig.27 the potential for achieving a high DD reaction rate is demonstrated. The DD fusion reactivity is plotted as a function of RF power for all the discharges in the series with $\omega=3\omega_{CD}$.
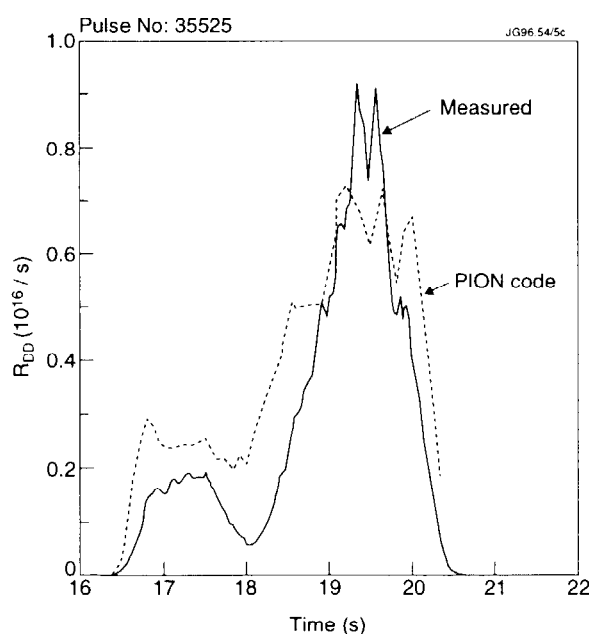

Fig. 26: Comparison between the measured DD reaction rate and that simulated by the PION code.
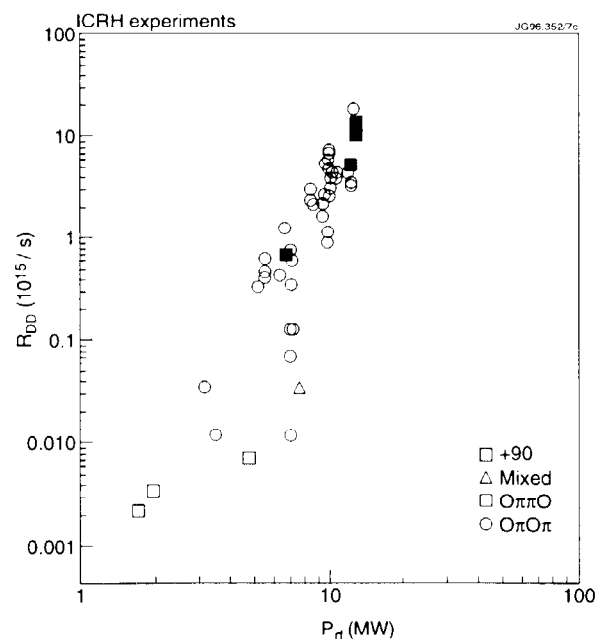
Fig. 27: Scaling of DD reactivity with ICRF power for the $3\omega_{CD}$ heating scheme.

Having validated the PION simulation with the measured neutron rate we now turn our attention to the power partition as given by the simulation. The calculated third harmonic deuterium absorption, direct electron absorption and parasitic absorption are shown in Fig.28. As we can see, the third harmonic damping becomes dominant quite early in the discharge while the direct electron damping remains low. This result is supported by the measurements of the direct damping on electrons in the centre of the plasma, which give a power density of $0.28MW/m^3$ in the plasma centre compared with the PION calculation of $0.24MW/m^3$.

Fig. 28: PION code calculation of the power flows to deuterium ions, electrons and parasitic absorption.

The scenario with $\omega = 3\omega_{CD}$ in the centre of a deuterium plasma has been used in TORE SUPRA to obtain good direct electron heating and TTMP current drive with no evidence for damping on the ions at the third harmonic resonance [30]. The difference could be due to the better confinement of the fast ions on JET which is supported by simulations with the PION code. When particle losses at relatively low energies (~800 keV) are introduced, then PION simulations give no significant enhancement of the third harmonic damping. The understanding of these PION code results suggests that the theoretical picture of the heating mechanism is correct, which gives confidence in predictions of future performance, especially for second harmonic tritium heating of DT plasmas in JET and ITER.

7. RF IN HOT-ION H-MODES

In JET the NBI produced ELM-free hot-ion H-mode plasma has generated the highest D-D fusion reaction rate and represents one of the leading modes for high fusion performance in the next tritium phase of operations [11]. The plasma configuration is characterised by a relatively high triangularity ($\delta \cong 0.25$), expanded flux surfaces in the divertor and low recycling: conditions which are not optimised for ICRH coupling. Recent modifications of the outer limiter has now greatly improved the ICRH coupling to hot ion H-modes and these results will be presented at a later date. During the last experimental campaign, a small number of hot-ion H-mode discharges were made with the addition of ICRH combined with NBI. We have found that when the ICRH is deposited centrally, the global thermal confinement of the plasma is increased by a factor of up to 30% compared with a control case with NBI only.
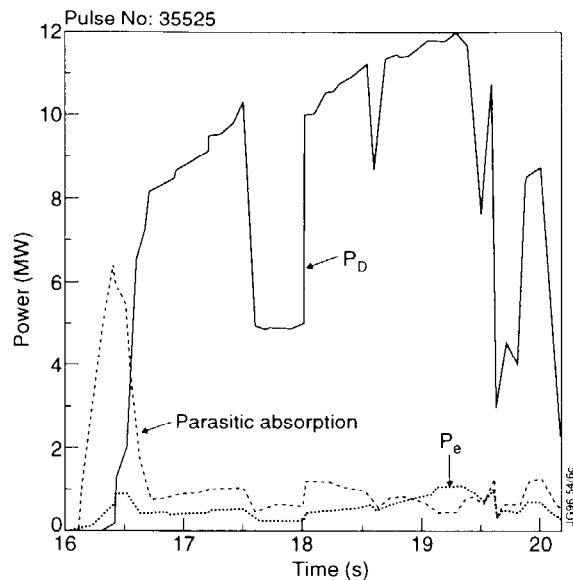
17

To illustrate this effect, two similar discharges with I_p = 3MA, B_T = 3.1T and q_{95} = 3.9 are compared in Fig.29. Discharge 34454 had both ICRF and NBI heating with up to 6MW of ICRH combined with 17MW of NBI. The control case with NBI alone, (discharge 34443), was heated with 18 MW of NBI only. In discharge 34454, the decrease in the coupled RF power from ~6 MW at the start of the main heating phase to ~2 MW at the time of the maximum neutron emission rate was caused by a decrease in the coupling resistance due to the plasma being moved away from the antenna (from 4cm to 10cm). In both discharges the central ion temperature,

Fig.29: Comparison between NBI and NBI + RF heating in hot ion, ELM-free H-modes.

$T_i(0)$, was in excess of 20 keV and both discharges had been pre-heated by similar LHCD powers in an earlier phase of the discharge. The LHCD has the effect of driving off-axis current, maintaining q(0) > 1, and suppressing MHD sawteeth prior to the main heating phase [31].
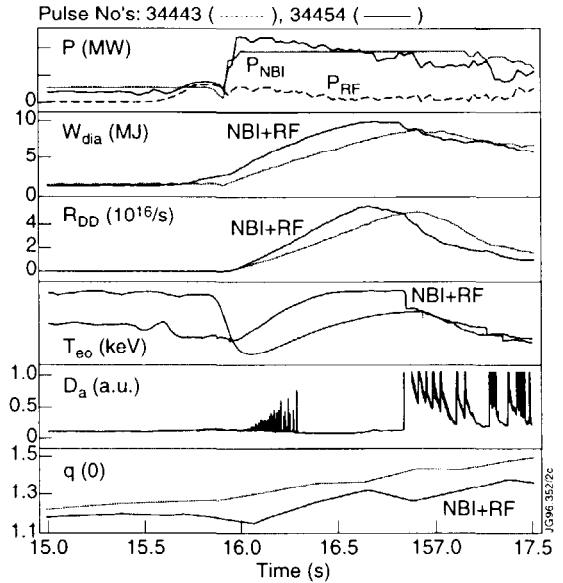
With combined heating, there is a clear enhancement in the D-D fusion reactivity as well as the total plasma energy content. The increased energy content is partly due to the increased heating power, partly to an enhanced thermal confinement time, and partly to the extra energy content of the ICRH fast ions which is measured by the diamagnetic loop. The maximum value of the perpendicular component of the fast ion energy in discharge 34454 is 2.9 MJ while the diamagnetic energy is 9.8MJ. The PION code has been used to estimate the fast ion content and this component has been subtracted from the measured diamagnetic energy to provide a magnetic measurement of the thermal stored energy. From this we have determined the thermal confinement time, which we have normalised to the ITERH93-P scaling law to derive the H-factor of enhancement. With the data normalised in this way, systematic differences due to the differences in input power are eliminated. The data are displayed in Fig.30 for the two pulses and show that the thermal H-factor is up to 30% larger during the combined heating case. In addition, we note that enhanced performance with combined heating is also obtained when LHCD is not applied. However, such discharges have poorer overall performance because the ELM-free periods are interrupted by sawteeth which limit the peak fusion yield.

To reveal the underlying cause of the improvement in global confinement, we have analysed in detail the thermal transport using the TRANSP code, based on measured diagnostic data. TRANSP simulations have been made of the two hot-ion H-mode discharges shown in Fig.29. In the simulations presented here, the ion temperature profiles were given by beam

18

charge-exchange recombination spectroscopy, and the electron temperature profile was derived from ECE emission data. The internal equilibrium calculated by TRANSP was used to map the ECE temperature data onto the major radial coordinate and thus ensure a high level of internal self-consistency between data and model. The electron density profiles used were from multi-point Thompson scattering (LIDAR) diagnostic.
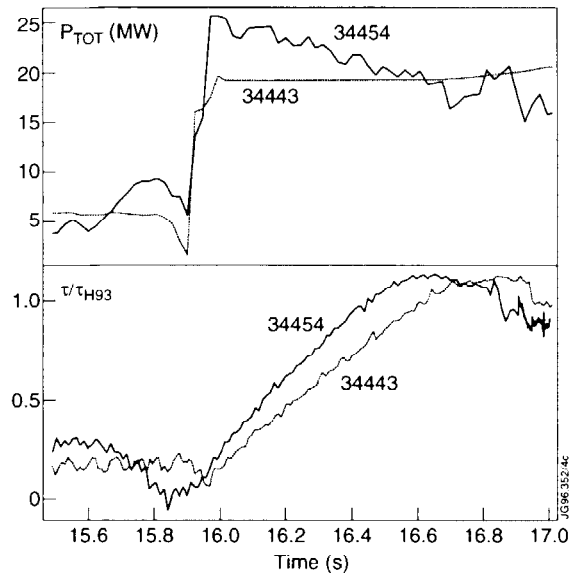

Fig.30: Confinement times referenced to ITER-H93P scaling for discharges 34454 (RF + NBI) and 34443 (NBI only).
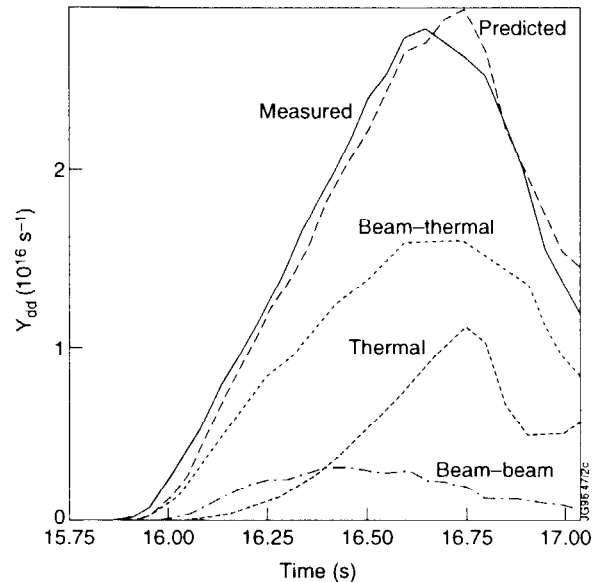
Fig.31: Comparison of measured neutron yield and TRANSP simulation for discharge 34454.

ICRF heating in discharge 34454 was in the hydrogen minority regime with the resonance close to the axis. The high-performance phase of the discharge was terminated by an ELM and a sawtooth collapse at time 16.83 seconds in the discharge. A sensitive measure of the quality of a TRANSP simulation is the degree to which the total neutron emission rate can be simulated given the other experimental data. The total 2.5 MeV D-D neutron emission rate is shown in Fig.31. The measured rate reaches a maximum of 2.8×10^{16} sec^{-1} at time 16.65 seconds, which is well simulated (to within approximately 3%) by the TRANSP model. At this time in the discharge 58% of the D-D neutron production arises from beam-thermal reactions, 32% from thermal deuterium reactions and 10% from beam-beam reactions. The ICRH model in TRANSP tracks the development of the energetic minority tail and its subsequent thermalization on the background ions and electrons using a Fokker-Planck description. Other wave damping mechanisms computed include damping at the deuterium second harmonic, the direct wave damping on the electrons (via TTMP and electron Landau damping) as well as mode conversion. However, the RF model currently in use does not compute the D-D fusion reactivity which can arise if a substantial and energetic deuterium tail, resulting from the second harmonic damping on either the NBI or the thermal deuterium, is produced. The good agreement obtained between the measured and predicted total neutron emission in Fig.31 shows

that any additional D-D fusion reactivity arising from the ICRF second harmonic interaction was relatively small in this discharge.

The enhanced confinement of the combined ICRF and NBI heated discharge could be explained by changes in the underlying quality of the thermal insulation of the plasma - the thermal diffusivity. However, as can be seen in Fig.32, TRANSP results show no significant difference in the derived electron thermal diffusivity. At time 16.7s and in the confinement region $(0.3 < r/a < 0.7)$, TRANSP shows similar values of the electron thermal diffusivity; $\chi_e \approx (0.4 \pm 0.2)$ m^2 s^{-1} for discharge 34454 and $\chi_e \approx (0.5 \pm 0.25)$ m^2 s^{-1} for discharge 34443. These values are typical of those obtained for the hot-ion H-mode in JET, and show that the enhancement in the global confinement found in the combined heating case with ICRH cannot be explained by a change in the thermal diffusivity.

A substantial difference between the combined heating and the beam-only discharges can, however, be seen in the heating profiles and could be a candidate explanation. Fig.33 shows the radial profiles of the volume-integrated heating rates separately for both the NBI and the ICRF heating. The ICRF heating profile is more peaked than that of the NBI. About 85% of the total ICRH power is found within a radius r/a = 0.4 whereas only 45% of the total NBI power is found in that region. We expect that the more localised central power deposition of the ICRH in a region where the thermal conductivity is low, will improve the central thermal energy content and also the global energy content. However, transport simulations of discharges 34443 and 34454 predict only an 8% improvement in the H-factor compared with the 30% measured increase.
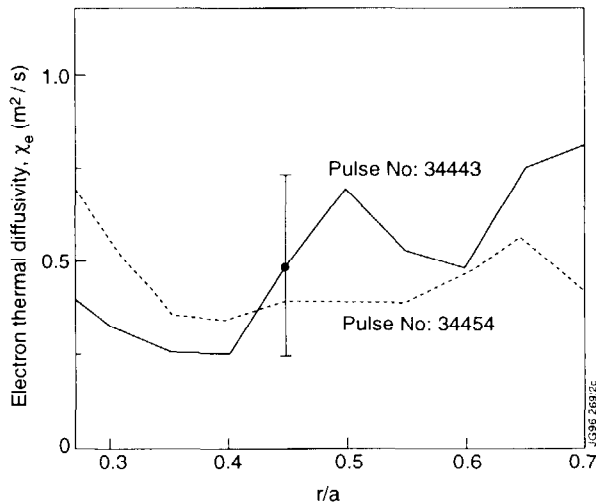

Fig. 32: TRANSP calculation of the electron thermal diffusivity profiles for discharges 34454 and 34443.
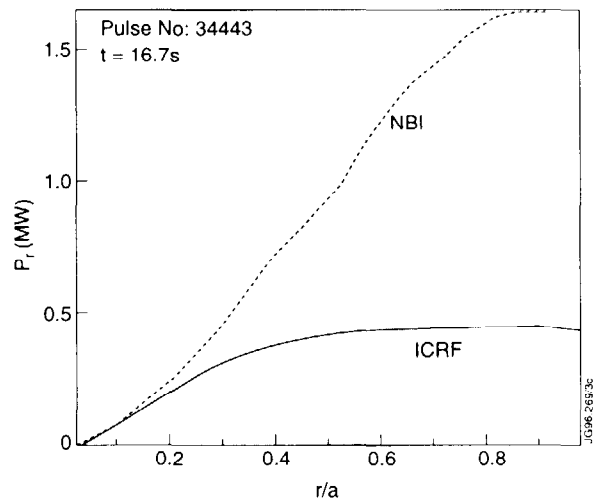
Fig. 33: TRANSP calculation of the power flow at a given radius versus the normalised radius r/a. Note the more peaked power deposition profile in the case of ICRH.

Another explanation which agrees better with the experimental results for the enhancement of the H-factor in hot ion H-modes can be found in the work of Bak et al [32]. These authors solve the heat diffusion equation with a neo-classical boundary condition at the separatrix. This boundary condition represents the transport barrier at the separatrix and is derived under the assumption that the energy losses in both the electron and ion channels are related to direct losses of banana ions across the separatrix. The important consequence is that the heat flux across the boundary, Q_L, is independent of the plasma temperature at the edge and is constant for constant edge density:

$$Q_L = kn^2(a).$$

Thus the global energy balance is given by

$$\frac{dW}{dt} = P - Q_L. \tag{3}$$

For a constant edge density, n(a), and input power P

$$W = W_0 + (P-Q_L)t, \tag{4}$$

where W_0 is the energy content at the time the edge transport barrier is formed. Thus the energy content increases linearly with time and never reaches a steady state. The global confinement time, defined as $\tau_E = W/(P-dW/dt)$ also increases with time,

$$\tau_E = \tau_0 + (P/Q_L - 1)\, t$$

where $\tau_0 = W_0/Q_L$.

From the ITERH93-P scaling given by equation (1) we see that, since Q_L is constant, τ_{93} is only weakly dependent on time through the evolution of the density. Thus the H-factor, H = τ_E/τ_{93}, is predicted to increase approximately proportional to time as is seen in Fig.30. Moreover the rate of rise depends on applied power, a feature which is also apparent in Fig.30. The rate of rise is given by:

$$\frac{dH}{dt} = \frac{1}{\tau_{93}}\left(\frac{P}{Q_L} - 1\right) \tag{5}$$

We estimate Q_L to be $\sim$ 10MW using equation 3 and the measured W(t) for discharge 34443. Using this value we calculate the fractional increase in dH/dt produced by the addition of ICRF in discharge 34454 and find that in this pulse the H-factor should increase 1.4 times more rapidly than in discharge 34443. This predicted increase agrees reasonably well with the observed ratio of 1.25 of the slopes between t = 16.0s and t = 16.5s shown in Fig.30.

Further optimisation is required in order to explore and realise the potential benefit of this plasma and heating configuration. To put things into perspective we have considered only the hot-ion H mode pulses at 3MA and assess performance simply in terms of achieved neutron emission rate. On these grounds the combined heating pulse 34454 ranks highly at 70% of the highest neutron emission discharge (pulse 34499). The latter pulse was NBI only but achieved its performance because the ELM-free period persisted considerably longer (1.36 sec) than in discharge 34454 (0.65 sec). Indeed, if we take the neutron emission rate in discharge 34499 at the same time (0.7 sec) after the commencement of the main heating power waveform, the performance with NBI only is poorer - only ~ 80% of the neutron emission - than in the case which includes ICRF. With lower recycling and improved stability [11], it is known that longer and higher performance than in 34443 is possible with NBI only. Adding ICRF/LHCD can certainly improve performance of the best NBI plasmas still further, provided the ELM-free period is maintained.

8. HIGH ELECTRON TEMPERATURES

An example of an RF H-mode that achieved 14.5keV central electron temperature has been described in section 3 and shown in Fig.7. A record electron temperature of 15keV has been produced by combined RF and NBI heating in a 3MA, 3.2T hot ion H-mode as shown in Fig.34. The H-mode is produced by 8MW of NBI which is then progressively stepped down. the RF power is ramped up and then remains constant at 4MW. As a result of the beam power step down both the stored energy and the density reach stationary values during the period of high confinement. The central electron temperature reaches 15keV at t = 18.2s for a central density of $4 \times 10^{19}m^{-3}$. The central ion temperature is 12keV at this time. The H-factor referenced to ITER89-P

Fig. 34: Hot ion H-mode with combined heating and NBI power step-down. The central electron temperature reaches 15keV.

confinement scaling attains values in the range H = 2.5 to H = 3 depending on whether the fast ion energy content is subtracted from, or included in W_{dia}.

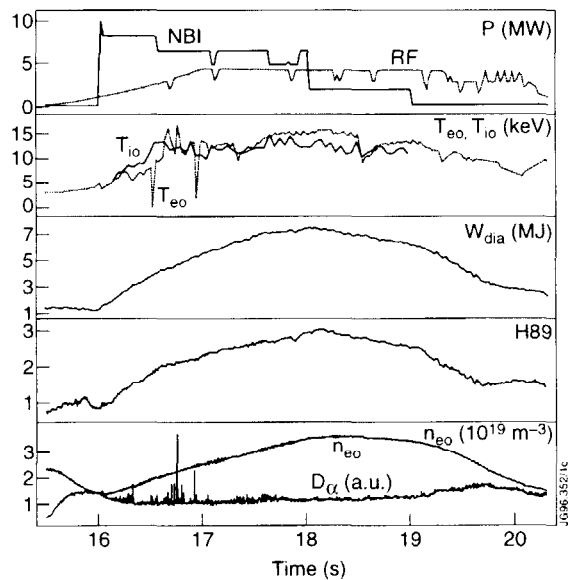The scaling of the central electron temperature with $P_{RF}/n_e(0)$ is plotted in Fig.35 for hot ion and RF H-modes in 3MA triangular configurations and also for RF-H-modes in 2.5MA discharges that simulate the JET "gas box" divertor configuration. For the hot ion cases the data

span only a small range in $P_{RF}/n_e(0)$. Consequently, the scaling is difficult to ascertain but the points lie in the same region as those from pellet enhanced performance H-modes (PEP + H) and hot electron modes obtained in the 1991/92 experimental campaign [33]. Figure 35 also shows for comparison the scaling of $T_i(0)$ with $P_{NBI}/n_e(0)$. In this case the beam power is taken as the scaling parameter since the beam predominantly heats the ions whereas the RF mainly heats the electrons. The equipartition term is small in the core of these plasmas. Note that similar values of $T_e(0)$ and $T_i(0)$ are obtained for the same values of power per particle implying that the electron and ion thermal conductivities in the core also have similar values.

The 3MA, RF-only H-modes show a linear dependence of Te(0) with $P_{RF}/n_e(0)$ up to a value $P_{RF}/n_e(0) = 3 \times 10^{-19} m^3 MW$. Above this value, $T_e(0)$ increases less rapidly perhaps due to fast ion orbit spreading of the electron heating profile or an adverse scaling of χ_e with temperature. A clear, non-linear behaviour is evident in the 2.5MA "gas box" divertor data in which $T_e(0)$ saturates at 9keV. Transport analysis has been carried out for several of the above discharges using the TRANSP code. Radial profiles of the thermal conductivity χ_e for the RF H-mode discharge 34046 and the hot ion H-mode, discharge 34242, at the time of maximum $T_e(0)$ are shown in Fig.36.

Fig. 35: Central electron and ion temperatures in hot ion H-modes and RF-only H-modes versus $P/n_e(0)$.

Fig. 36: Thermal conductivity profiles from TRANSP analyses for the various types of discharge represented in Fig. 34.

The values of χ_e for the hot ion H-mode are about a factor of two lower than those of the RF H-mode over most of the plasma minor radius. In the case of the 2.5MA "gas box" divertor plasmas with the highest $P/n_e(0)$ radius, the values of χ_e in the core region are about twice as
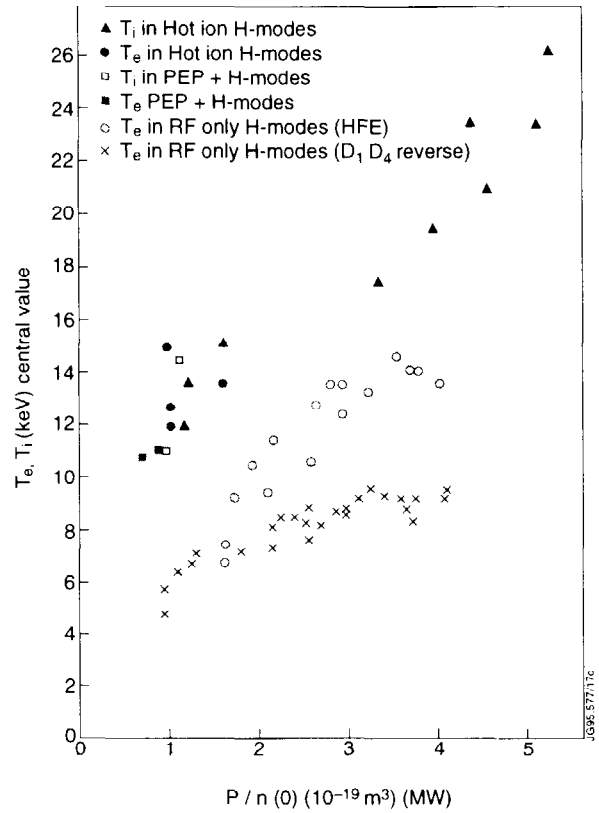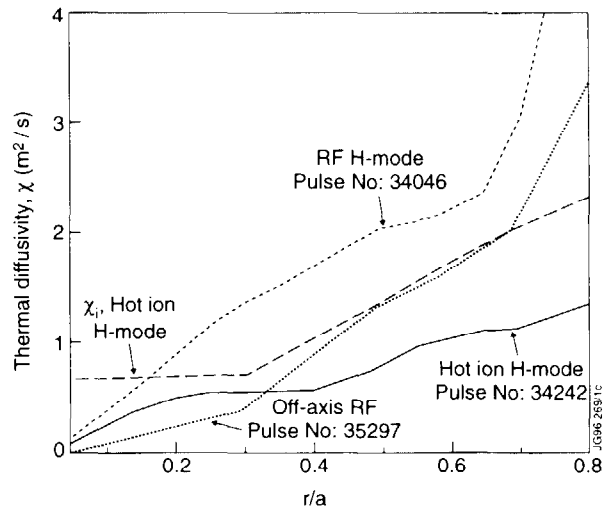
large as those for the RF H-mode; typically $\chi_e(r/a = 0.3) \sim 3m^2/s$. For the hot ion H-mode the ion thermal conductivity χ_i is typically 50% larger than χ_e

As the electron temperature increases, (and hence the electron beta), the fraction of power absorbed directly by the electrons by combined electron Landau damping and transit time magnetic pumping also increases. This effect helps to concentrate the power deposition in the plasma centre and counteracts the orbit-broadening of the fast ion heating profile as the high power levels produce fast ions in the MeV energy range. An example is shown in Fig.37 where the central electron beta is seen to be a factor of two greater in the hot ion H-mode compared to that in the RF-only H-mode case. Also shown are the ratios of ELD + TTMP to minority cyclotron damping rates obtained from a PION simulation. In discharge 34242 the volume integrated direct electron damping reaches 15% of the input power compared with 6% in discharge 34046.

An interesting variation of the 3MA discharges was discharge 35297 in which the ICRF resonance layer was 0.3m on the high field side of the magnetic axis. Even so 5MW of RF power produced a central electron temperature of 10keV at a density $n_e(0) = 2.7 \times 10^{19}m^{-3}$ (Fig.38). This electron temperature is higher than the values achieved for the same power per particle with a central resonance in the 3MA RF-only H-modes as shown in Fig.35. Transport analysis shows that χ_e is similar to that for the hot ion H-mode over the inner half of the minor radius and about a factor of two less than that for the RF-only H-mode in the same region.
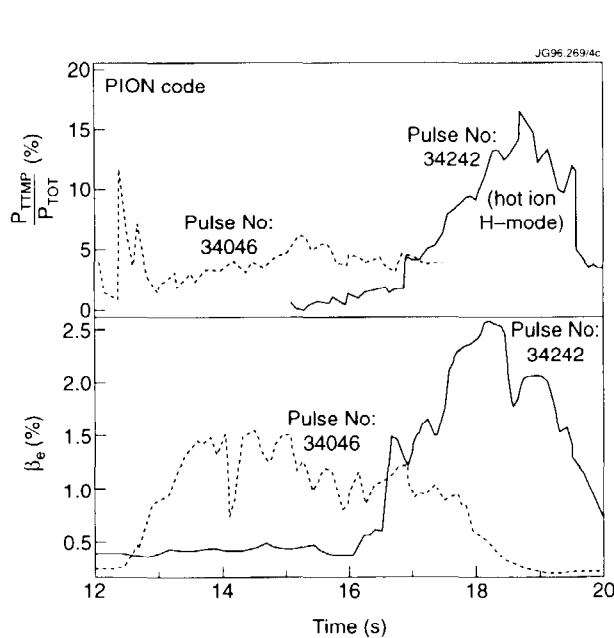

Fig. 37: Correlation between the power fraction absorbed by TTMP, as calculated by the PION code, and the measured central electron beta.
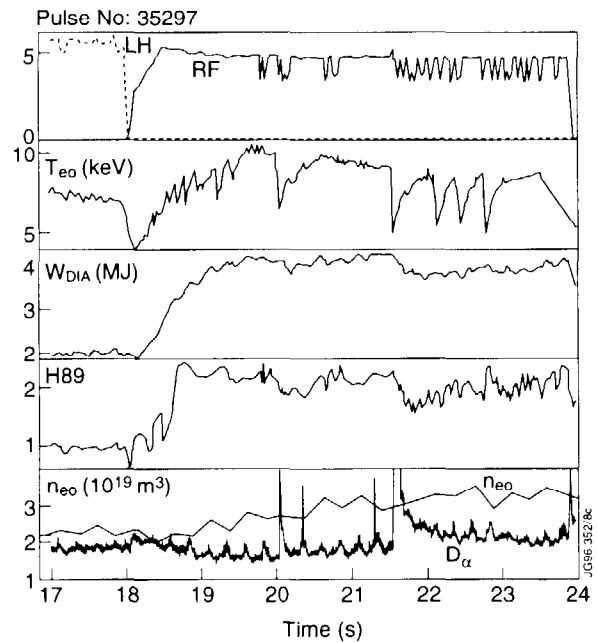
Fig. 38: RF-only H-mode with off axis ICRH which produced 10keV central electron temperature.

24

9. SUMMARY

Ion cyclotron resonance heating on JET has been applied to a variety of H-mode plasmas with up to 16.5MW of coupled power. In a 5MA discharge a plasma stored energy of 7MJ has been achieved with 8.5MW of central hydrogen minority heating. Combined ICRF and NBI heating up to 32MW has been used to form and study high density strongly radiating divertor plasmas in which the H-factor was improved by the localised central RF power deposition. The observed enhancement in the normalised global confinement time agrees well with thermal transport simulations in which the conductivity is take to vary as $\chi \propto T^2$ as implied by ITERH93-P scaling.

Studies of plasma rotation at $r/a \sim 0.3$ during ICRH have shown a strong acceleration of the plasma immediately after the H-mode is formed. This effect is interpreted as a step increase in the momentum confinement analogous to the steps in energy and particle confinement at the L-H transition. The magnitude and direction of the acceleration are consistent with the ion pressure gradient being the major part of the driving torque, with the RF providing a small counteracting component.

H-mode threshold measurements with ICRF has shown similar values to those achieved with NBI. There data fit the scaling laws $P_{TH} = 0.025 \; n_e B_t S$ and $P_{TH} = 0.3 n_e B_t R^{2.5}$ almost equally well.

Non thermal D-D fusion reactions with a rate of $2 \times 10^{16} s^{-1}$ have been generated by third harmonic heating of the majority deuterium ions without the need for initial tail formation by NBI. A good simulation of the time development of the reactivity has been obtained with the PION code which gives good confidence in the predictions of this code for other scenarios such as second harmonic tritium heating in D-T plasmas.

The injection of fast waves into hot ion H-modes has increased the normalised thermal energy content by up to 30% compared with that achieved by beam heating alone. Transport analysis with the TRANSP code established that there is no change in the thermal conductivity. The effect is too large to be produced by the centrally localised nature of the ICRH for which transport simulation predict an increase of 8%. The enhancement is consistent with an interpretation in terms of an edge confinement barrier which maintains an energy loss which is independent of the plasma energy content. With this boundary condition the H-factor increases with time at a rate which increases with the input power.

Central electron temperatures close to 15keV have been obtained in both RF-only and hot ion H-modes. This value is close to the anticipated electron temperature in ITER at ignition, namely $T_e(0) = 19keV$. The temperature gradient and the electron toroidal beta are also similar to the expected values in ITER, but the density in JET is three times lower as shown in Table 1. The power required to improve the electron temperature to the ITER value depends on the scaling of χ_e. All these data indicate that ICRH as a heating method compares very

favourably with NBI heating, especially when its basic advantages; central heating independent on density and no fuelling at the edge, are fully exploited.

Table 1: Comparison of JET and ITER Parameters

	T_e (keV)	∇T_e (keV m^{-1})	β_e (%)	β_{fast} (%)	n_e (10^{20}m^{-3})
JET	15	18	2.5	1.7	0.4
ITER	19 (Ignited)	15	3.2	0.7	1.3

REFERENCES

[1]   Bhatnagar V P, et al, Plasma Physics and Controlled Fusion 33 (1991)99.

[2]   Gehre, O, et al. Proc. of 22nd EPS Conference on Controlled Fusion and Plasma Physics, Bournemouth, UK, 1995. Vol.19c part 1, p.20.

[3]   Challis C D, et al, Proc. of 22nd EPS Conference on Controlled Fusion and Plasma Physics, Bournemouth, UK 1995, Vol.19c, part 2, p.69.

[4]   Jacquinot, J and the JET Team, 33 (1991) 1657.

[5]   Prater R, et al, Proc. of 22nd EPS Conference on Controlled Fusion and Plasma Physics, Bournemouth, UK, 1995, Vol.19c, part 1, p.381.

[6]   Petty C C, et al. Proc. of 15th IAEA Int. Conf. on Plasma and Controlled Nuclear Fusion Research, Seville, Spain, 1994, Vol.2, p.211.

[7]   Equipe Tore Supra, Proceedings of 15th IAEA Conference on Plasma Physics and Controlled Nuclear Fusion, Seville, Spain 1994, paper CN-60/A3/5-P-7..

[8]   Majeski R, et al. Proc. of 22nd EPS Conference on Controlled Fusion and Plasma Physics, Bournemouth, UK, 1995, Vol..19c, part 2, p.365.

[9]   Bhatnagar, V P, et al, Nuclear Fusion 34 (1994) 1579.

[10] Kaye A S, et al. Proc. of the 16th IEEE/NPSS Symposium on Fusion Engineering, Champaign, USA 1995, to be published.

[11] Jones T T C, et al. Plasma Physics and Controlled Fusion, 37 (1995) 359.

[12] Start, D F H, et al. Proc. of the 11th Topical Conf. on Radio Frequency Power in Plasmas, Palm Springs, USA, 1995, p.7.

[13] Bertolini, E. Proc. of 16th IEEE/NPSS Symposium on Fusion Engineering, Champaign, USA 1995, to be published.

[14] Start, D.F.H et al, Proc. of IAA Tech. Comm. on Fast Wave Current Drive in Reactor Scale Tokamaks, Arles, France, 1991, p.227..

[15] Bures M., et al, Proc. of 21st EPS Conference on Controlled Fusion and Plasma Physics, Montpelier, France 1994, Part II, p.944.

[16] Bickley, A, private communication.

[17] V.P. Bhatnagar, et al, Nuclear Fusion 24 (1984), 955.

[18] Bartiromo R , et al. Rev. Scie.. Inst. 60(1989) 237.

[19] Eriksson L G, Righi E and Zastrow K D, to be submitted to Nuclear Fusion.

[20] Hazeltine, R.D., Meiss, J.D., Plasma Confinement. Addision Wesley, 1992.

[21]. Hinton, F.L., Robertson, J.A., Phys. Fluids 27 (1984) 1243.

[22] Hellsten, T., Plasma Physics and controlled Fusion 31 (1989) 1391.

[23] Parail V.V. et al, Proceedings of 22nd EPS Conference on Controlled Fusion and Plasma Physics, Bournemouth, UK, 1995. Vol.19C, part 1, p.13.

[24] Ryter F, and the H--mode Database Working Group, JET report JET-P(95)55, to be published in Nuclear Fusion.

[25] Seki, T, et al., Nuclear Fusion 31, 1369 (1991).

[26] Imai, T. et al., in Plasma Physics and Controlled Nuclear Fusion Research (Proc. 13th Int. Conf. Washington DC, 1990) IAEA-CN-53/E-I-3, Vol.1., IAEA, Vienna (1991) 645.

[27] Korotov, A.A., Gondhalekar, A, and Stuart A.J, accepted for publication in Nuclear Fusion,

[28] Eriksson, L.-G., Hellsten, T. and Willén, U., Nuclear Fusion 33, 1037 (1993).

[29] Eriksson, L.-G., and Hellsten, T., Physica Scripta 52, 70 (1995).

[30] Equipe TORE SUPRA in Plasma Physics and Controlled Nuclear Fusion Research (Proc. 15th Int. Conf. Seville, Spain 1994) IAEA-CN-60/A3-6, Vol.1, IAEA, Vienna (1994) 461.

[31] Fischer B., et al, Proc. of 22nd EPS Conference on Controlled Fusion and Plasma Physics, Bournemeouth, UK, 1995, Vol.19C, part III, p.361.

[32] Bak, P. et al, JET report JET-P(95)09, submitted to Nuclear Fusion.

[33] Tubbing B.J.D. et al, Nuclear Fusion 31 (1991), 839.